Supporting Information

Parallel and perpendicular alignment of anisotropic particles in free liquid micro-jets and emerging micro-droplets

Mathias Schlenk[a], Eddie Hofmann[a], Susanne Seibt[a], Sabine Rosenfeldt[a,d], Lukas Schrack[b], Markus Drechsler[a,d], Andre Rothkirch[e], Wiebke Ohm[e], Josef Breu[c,d], Stephan Gekle[b], Stephan Förster[a]

[a] Physical Chemistry I, University of Bayreuth, 95440 Bayreuth, Germany.

[b] Biofluid Simulation and Modeling, University of Bayreuth, 95440 Bayreuth, Germany.

[c] Inorganic Chemistry I, University of Bayreuth, 95440 Bayreuth, Germany.

[d] Bavarian Polymer Institute, University of Bayreuth, 95440 Bayreuth, Germany.

[e] HASYLAB/DESY, 22607 Hamburg, Germany.

Corresponding Author:

Stephan Förster
JCNS-1/ICS-1, Forschungszentrum Jülich, D-52425 Jülich, Germany
Phone: +49 2461 61 85161, Fax: +49 2461 61 2610,
Email: s.foerster@fz-juelich.de

Microfluidic Device

All micro-jet experiments were performed using a newly developed microfluidic setup that allows to cycle small liquid volumes at high flow rates to continuously generate stable micro-jets. The microfluidic setup consists of a micro annular gear pump (mzr-7205G, HNP Mikrosysteme GmbH) with an electrical control terminal box (S-G05) to precisely adjust flow rates as visible in Figure S1a. The pump is connected with silicone tubes to a specially fabricated 3D-printed sample holder which was designed in AutoCAD 2013 (Autodesk) and printed in polylactide using an Ultimaker 2 (Ultimaker B.V.). The 3D-printed sample holder was fabricated to hold a micro glass capillary (Hilgenberg GmbH) with an inner diameter of 600 µm (wall thickness 50 µm) and is constructed for long-time small angle X-ray scattering (SAXS) measurements at synchrotrons as it is shown in Figure S1b-d.

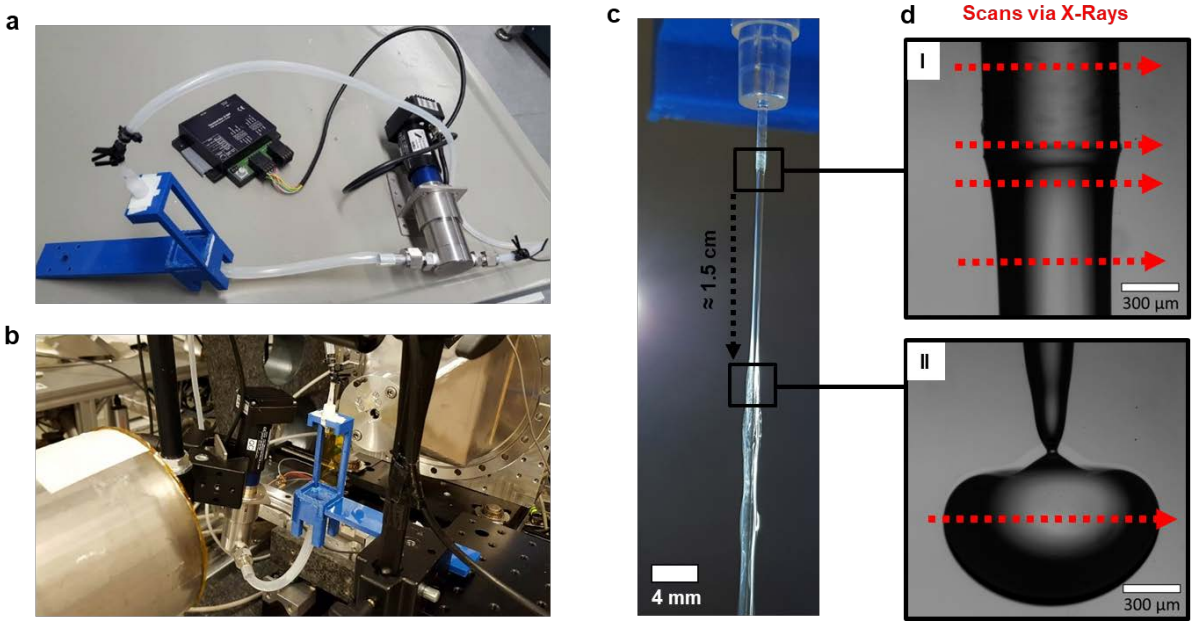

Fig. S1 Overview about the whole microjet setup. (a) 3D-printed sample holder (blue) and micro annular gear pump with control module. (b) Setup generating the microjet with a gear pump (7205G) at the synchrotron DESY, Petra III, beamline P03. (c) Video snapshot of the microjet indicating the nozzle exit as well as the droplet breakup area further downstream. Due to the extreme high flow rates and the high shutter speed of a normal camera, no drop formation is visible. (d) The droplet breakup is just visualized by a high speed camera that can run very short exposure times between each picture, whereby the SAXS positions for scans at the nozzle exit are shown at the top image (I) and at the droplet breakup area 1.5 cm further downstream at the bottom image (II).

Determination of the droplet breakup position

Figure S2 shows the position for the droplet breakup at ~ 13 mm downstream the glass capillary with diameter of *ID* = 600 µm and a flow rate of *Q* = 750 mL/h that is used during the SAXS experiments. Shown in the top row (Figure S2a) is a series of 20 subsequent 0.7 ms-snapshots of droplet breakups. Here we observe just a slight variation of the position for the droplet breakup between 0.5 – 1 mm at short time scales. The bottom row (Figure S2b) illustrates the droplet breakup over longer time scales of 1 second intervals. We observed just a small deviation from the droplet position of around 0.5 – 1 mm. All measurement positions were double checked by video microscopy to be sure about being either in the continuous jet or in the droplet regime (15.2 mm).

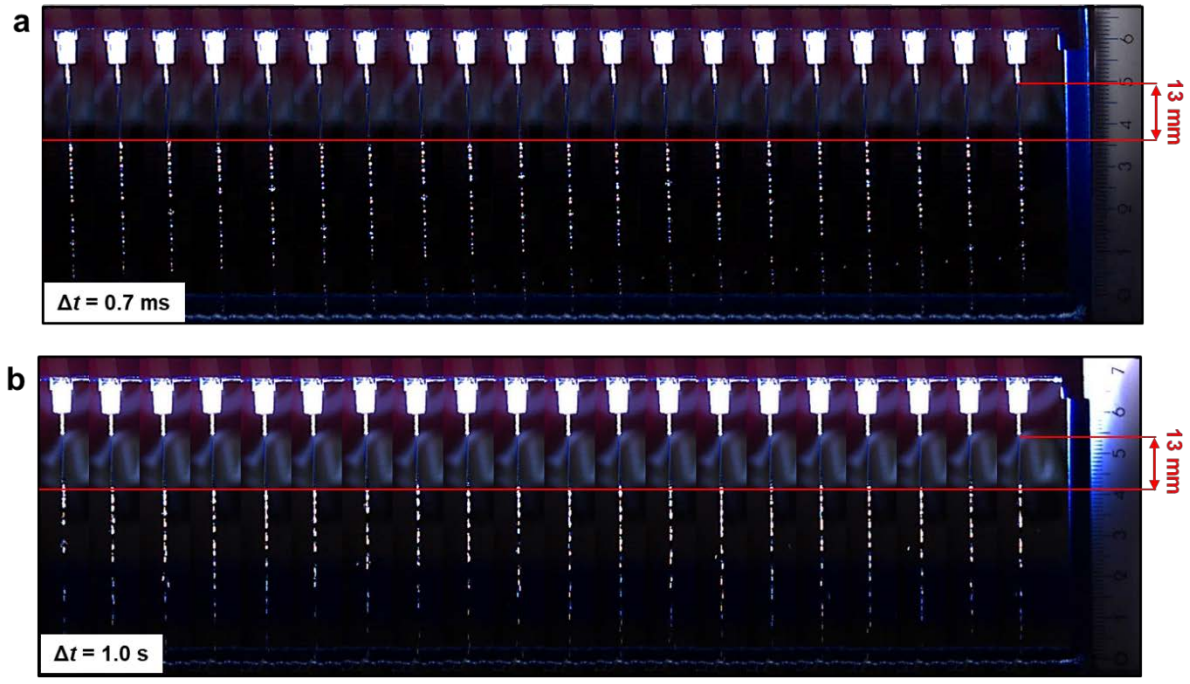

Fig. S2 Determination of the droplet breakup position. (a) Image series of the droplet breakup position for a capillary with diameter of *ID* = 600 µm and a flow rate of *Q* = 750 mL/h for short time intervals of Δt = 0.7 ms and (b) longer time intervals of Δt = 1.0 s.

Characterization of anisotropic particles

The liquid micro-jet setup has been run with three different types of anisotropic particles. Cryo-TEM and TEM-images are shown in Figure S3. The first sample, 1% w/w sodium hectorite nanoplatelets dispersion in water, is visible in Figure S3a. The 10% w/w of wormlike micelles solution and the dispersed gold nanorods are illustrated in Figure S3b, c.

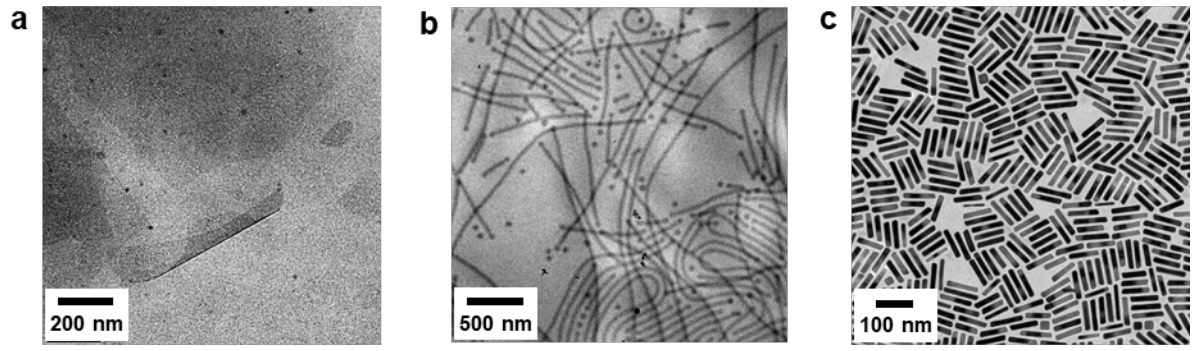

Fig. S3 Characterization of anisotropic particles via transmission electron microscopy. (a) Cryo-transmission electron microscopy (Cryo-TEM) image of $Na_{0.5}$-hectorite nanoplatelets with a concentration of c = 1% w/w in water. The sample was milled by ultrasonic treatment to shorten the originally aspect ratio of 20.000. (b) Cryo-TEM image of PI_{110}-PEO_{198} wormlike micelles solution with a concentration of c = 0.1% w/w in water. (c) Transmission electron microscopy (TEM) image of single crystal gold nanorods (Au-Nanorods).

Microparticle Image Velocimetry

To determine the velocity profile experimentally, we used microparticle image velocimetry (µPIV). The setup consists of a Phantom v1612 high-speed camera (Vision Research), and a highly intense, focused light source Halolux LED-30 (Streppel Glasfaser-Optik oHG). In combination with a Model K1 CentriMax^{TM} long distance microscope (Infinity Photo-Optical Company) and a 10x /0.30 P UPlanFL N magnification objective (Olympus Corporation) the setup allows exposure down to 1.5 µs and frame rates up to 210,000 s^{-1} for the performed experiments. Due to the narrow depth of focus of this kind of setup a precise vertical position control within the microjet is possible. The sample-holder was adjusted in the way that the focus distance was always set to the inner center part of the microjet and just frames of that position are taken by the high-speed camera. In total, always 30 frames are taken from exactly the same position at the center for averaging. For data collection via high-speed camera measurements the Phantom PCC v2.8.761.0 software was used. The obtained high-speed image sequence is autocorrelated and analyzed using the open-source software package JPIV. Measurements were made in pure water that contained 0.1% w/v of 4.89 µm diameter monodisperse polystyrene tracer particles (Micro Particles GmbH). The results as well as analysis of the water microjet flow profiles based on a 300 µm diameter glass capillary and the generally used flow rate of 750 ml/h is shown in Figure S4.

Concerning the µPIV experiments, analysis problems appear due to light reflexions on the curved outer free jet but especially at the curved glass capillary. As a consequence, dark areas at the edge of the glass capillary are emerging and no valid evaluation within these black regions is possible by the software since the particles are not visible anymore for tracing. However, flow profile analysis for the freejet area is possible up to a certain point. The black area is just present at the outermost edge of the freejet and thus we can determine most of the flow profile. In Figure S4a, the freejet position 5 mm after outlet is analyzed via JPIV whereby the red marked jet edges of the dark regions are not considered. The results in Figure S4b are showing a velocity profile which is like plug flow with an average velocity of around $v_{average}$ = 2.0 m/s, whereby the zero velocity directly at the edge of the freejet is not available. Additionally, we have simulated the flow profile out of a capillary with a diameter of D = 30 µm and a flow rate of Q = 10 µL/h at the freejet area which is visible in Figure S4c. Here, a whole plug flow profile is recognized and matches quite good to the analyzed part of the experimentally found flow profile for the freejet area. Moreover, the flow profile within a capillary has also been simulated for the same parameters and the expected parabolic flow profile was determined, as seen in Figure S4d. However, a detailed analysis of an experimental flow profile is not possible due to intense light reflexions at the glass capillary. Nevertheless, a changing from a parabolic flow profile within the capillary to a plug flow profile within the freejet is identifiable by simulations and supported by experimental data. Consequently, this drastic change of the flow profile benefits the loss of orientation within and along the free jet.

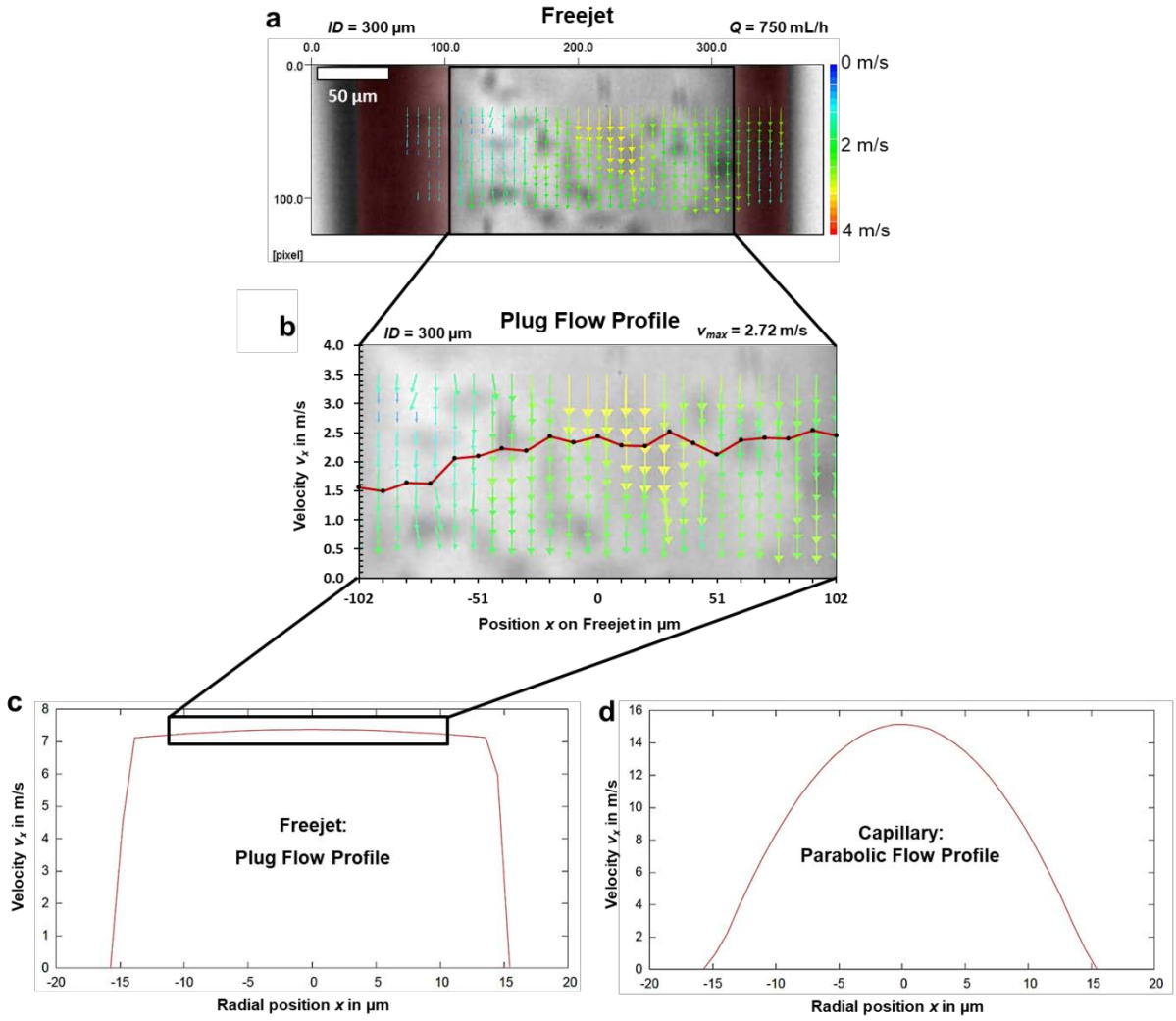

Fig. S4 Microparticle image velocimetry. (a) µPIV measured flow profile of water including monodisperse polystyrene tracer particles which are jetting out of a glass capillary with an inner diameter of 300 µm and flow rate of Q = 750 mL/h. The measurement position is on the freejet 5 mm after outlet. (b) Graph of analyzed plug flow profile with velocity Vx [m/s] versus position x on freejet in [µm]. (c) Simulated plug flow profile of the freejet out of a capillary with diameter of 30 µm and flow rate of 10 µL/h. (d) Simulated parabolic flow profile within the capillary and same flow rate.

In the further µJPIV experiments, we present the flow profile generated by a smaller 200 µm diameter glass capillary to show the influence of the microjet diameter and velocity on the flow profile. In Figure S5, the flow profile for the experimental flow rate of v = 750 mL/h is shown for different positions on the microjet. As discussed before, the vector arrows in the dark areas of the capillary and freejet of Figure S5 are not allowed to incorporate to the consideration. Though the black areas are present at the edge of the capillary and freejet, we at least can observe a parabolic flow profile within the glass capillary (Figure S5a) and the gradual growing

plug flow profile for the freejet at 5 mm after outlet (Figure S5b). As visible, the maximum velocity at the center part within the capillary amounts to v_{max} = 3.91 m/s and shows a parabolic flow profile in comparison to the rather plug flow profile for the freejet area at 5 mm after outlet, where the velocity decreased down to v = 3.16 m/s. Compared to the bigger capillary in Figure S4, the maximum velocity within the smaller capillary is much higher.

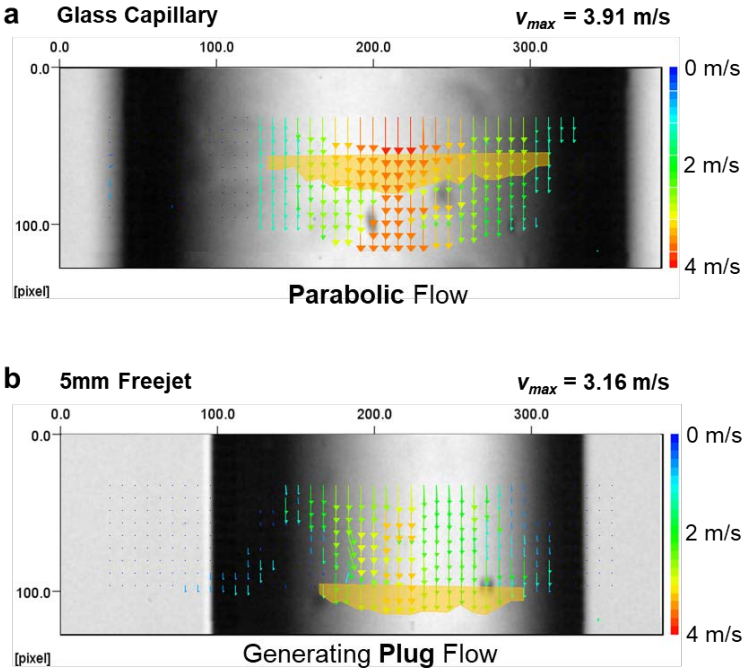

Fig. S5 µPIV measured flow profiles of water using monodisperse polystyrene tracer particles and a flow rate of v = 750 mL/h. a) Within a glass capillary of a diameter of ID = 200 µm and b) 5 mm after the outlet within the free jet.

SAXS-pattern calculation

In the following we outline the calculation of the scattering patterns of oriented anisotropic particles, such as cylinders and disks, which are dispersed in a solvent. For such two-phase systems consisting of particles (phase "1") with scattering length b_1 and volume fraction ϕ_1 in a solvent (phase "2") of scattering length b_2 and a volume fraction $\phi_2 = 1 - \phi_1$, separated by sharp interfaces, the scattered intensity per unit volume is given by

$$I(\mathbf{q},\mathbf{L},\mathbf{R}) = (b_1 - b_2)^2 \rho_N \left\langle \left\langle F^2(\mathbf{q},\mathbf{L},\mathbf{R}) \right\rangle_{L,R} \right\rangle_{or} \left[1 + \beta(\mathbf{q},\mathbf{L},\mathbf{R}) \left(\left\langle Z(\mathbf{q},\mathbf{g}) \right\rangle_{or} - 1 \right) G(q,g) \right] \quad (1)$$

where $\mathbf{q}$ is the scattering vector, $\rho_N = N/V$ is the number density of the particles, $F(\mathbf{q})$ the scattering amplitude or Fourier transform of the particle form, L is equal to the length of the

cylinder or the thickness of the sheet, R is equal to the cross-sectional radius of the cylinder or the lateral radius of the disk, $Z(\mathbf{q})$ is the lattice factor describing the spatial distribution of the particles, $G(q)$ is the Debye-Waller factor, and

$$\beta(\mathbf{q},\mathbf{L},\mathbf{R}) = \frac{\left\langle \left\langle F(\mathbf{q},\mathbf{L},\mathbf{R}) \right\rangle_{L,R}^{2} \right\rangle_{or}}{\left\langle \left\langle F^{2}(\mathbf{q},\mathbf{L},\mathbf{R}) \right\rangle_{L,R} \right\rangle_{or}} \tag{2}$$

The effect of the ratio $\beta(\mathbf{q})$ on the scattering intensity is similar to the effect of the Debye-Waller factor $G(q)$, resulting in a decay of the Bragg peak-intensities with increasing scattering vector q. Equation (1) considers the effect of the particles - via their first and second moment of the particle size distribution - and of the lattice - via the first and second moment of the distribution of lattice points - on the scattered intensity $I(q)$.

The scattering amplitude $F_C(\mathbf{q},\mathbf{L},\mathbf{R})$ for cylindrical particles of cross-sectional radius R and length L can be factorized into

$$F_C(\mathbf{q},\mathbf{L},\mathbf{R}) = F_{C\parallel}(\mathbf{q},\mathbf{L})F_{C\perp}(\mathbf{q},\mathbf{R}) \tag{3}$$

where $F_{C\parallel}(\mathbf{q},\mathbf{L})$ is the longitudinal contribution parallel to the cylinder axis, and $F_{C\perp}(\mathbf{q},\mathbf{R})$ is the contribution from the cross-section of the cylinder. $\mathbf{L} = L\mathbf{l}_{\parallel}$ is a vector with length L and a direction given by the unit vector parallel to the cylinder axis $\mathbf{l}_{\parallel}$. $\mathbf{R} = R\mathbf{I}_{\perp}$ is a vector with length R and a direction given by the unit vector perpendicular to the cylinder axis $\mathbf{I}_{\perp}$. The directions are shown in Figure S6. The longitudinal and cross-sectional contributions for cylinders are given by

$$F_{C\parallel}(\mathbf{q},\mathbf{L}) = \frac{\sin(\mathbf{qL}/2)}{\mathbf{qL}/2} \tag{4}$$

$$F_{C\perp}(\mathbf{q},\mathbf{R}) = \frac{2\,\mathrm{J}_1(\mathbf{qR})}{\mathbf{qR}} \tag{5}$$

where $\mathrm{J}_1(z)$ is the Bessel function of the first kind.

The structure of disks can be described by their lateral radius R_D and the thickness D as shown in Figure S6.

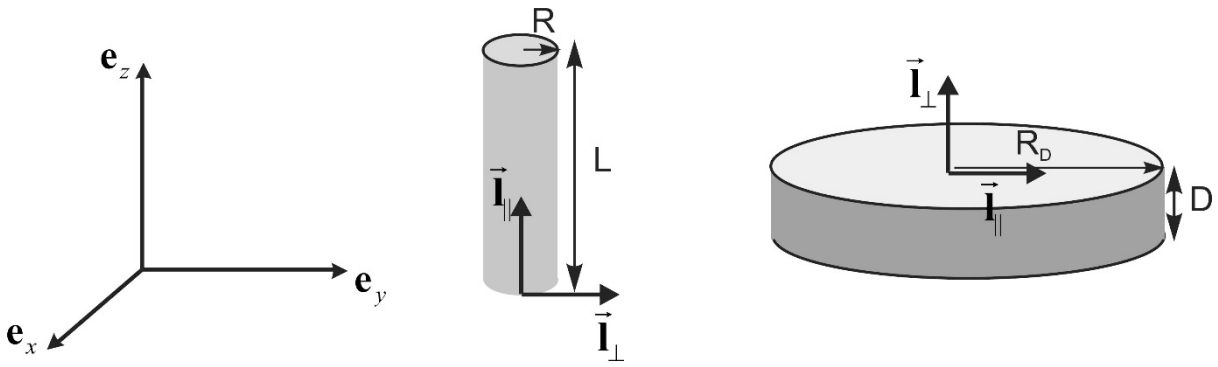

Fig. S6 Different shapes used for SAXS-pattern calculation. Definition of directions for cylinders and disks to calculate the longitudinal and cross-sectional formfactors.

Since disks could equivalently be considered to be short cylinders, where the cross-sectional radius R is larger than the length L, the scattering amplitudes can be derived by substituting $\mathbf{L} \to \mathbf{D}$ and $\mathbf{R} \to \mathbf{R}_D$ in Equation (3-5) to obtain

$$F_D(\mathbf{q}, \mathbf{D}, \mathbf{R}_D) = F_{D\|}(\mathbf{q}, \mathbf{R}_D) F_{D\perp}(\mathbf{q}, \mathbf{D}) \tag{6}$$

where $F_{D\|}(\mathbf{q}, \mathbf{R}_D)$ is now the contribution in the lateral direction and $F_{D\perp}(\mathbf{q}, \mathbf{D})$ is the contribution from the cross-section of the disk. The normal and cross-sectional contributions for disks are given by

$$F_{D\|}(\mathbf{q}, \mathbf{R}_D) = \frac{2\,\mathrm{J}_1(\mathbf{q}\mathbf{R}_D)}{\mathbf{q}\mathbf{R}_D} \tag{7}$$

$$F_{1\perp}(\mathbf{q}, \mathbf{D}) = \frac{\sin(\mathbf{q}\mathbf{D}/2)}{\mathbf{q}\mathbf{D}/2} \tag{8}$$

For the calculation of the averages over the size distribution of lengths L and radii R the scattering amplitudes can be factorized and integrated with respect to each of the variables $X = L, R$. In many cases, the Schulz-Zimm distribution is a useful size distribution function. Then the measured z-averages of the functions $f(q, X)$ are given by

$$\left\langle f(q, X) \right\rangle_X = \int_0^\infty f(q, X) X^m h(X) dX \tag{9}$$

with

$$h(X) = \frac{(z+1)^{z+m+1} X^z}{\overline{X}^{z+m+1} \Gamma(z+m+1)} \exp\left[-(z+1) \frac{X}{\overline{X}} \right] \tag{10}$$

with m the weighting factor for the variable X, the average $\overline{X}$, and the relative standard deviation $\sigma_X = (z+1)^{-1/2}$. The distribution is normalized such that $\int_0^\infty X^m h(X)dX = 1$. The weighting factor relates to the measured intensity being the z-average, such that for spheres $m = 6$, for cylinders $m = 2$ for the length, and $m = 4$ for the cross-sectional radius, and for disks $m = 2$ for the thickness and $m = 4$ for the lateral disk radius.

The orientational distribution of the particles can be obtained by averaging the scattering amplitudes $\langle F(\mathbf{q},\mathbf{L},\mathbf{R})\rangle_{L,R}$, $\langle F^2(\mathbf{q},\mathbf{L},\mathbf{R})\rangle_{L,R}$, $\langle F_D(\mathbf{q},\mathbf{D},\mathbf{R}_D)\rangle^2_{D,R_D}$ and $\langle F_1^2(\mathbf{q},\mathbf{D},\mathbf{R}_D)\rangle_{D,R_D}$ over a distribution of angles β between the cylinder axis or lateral direction of the disk, $\mathbf{l}_\parallel$, and the scattering vector $\mathbf{q}$. The relevant scalar products are $\mathbf{qL} = L\mathbf{ql}_\parallel = qL\cos\beta$, $\mathbf{qR} = R\mathbf{qI}_\perp = qR\sin\beta$, $\mathbf{qD} = D\mathbf{ql}_\perp = qD\cos\beta$, and $\mathbf{qR}_D = R_D\mathbf{ql}_\parallel = qR_D\sin\beta$. The orientational averages are then calculated as

$$\left\langle\left\langle F_C(\mathbf{q},\mathbf{L},\mathbf{R})\right\rangle^2_{L,R}\right\rangle_{or} = \int_0^{\pi/2}\left\langle F_{C\parallel}(qL\cos\beta(\delta))\right\rangle^2_L\left\langle F_{C\perp}(qR\sin\beta(\delta))\right\rangle^2_R h(\delta)\sin\delta d\delta \qquad (11)$$

$$\left\langle\left\langle F_C^2(\mathbf{q},\mathbf{L},\mathbf{R})\right\rangle_{L,R}\right\rangle_{or} = \int_0^{\pi/2}\left\langle F^2_{C\parallel}(qL\cos\beta(\delta))\right\rangle_L\left\langle F^2_{C\perp}(qR\sin\beta(\delta))\right\rangle_R h(\delta)\sin\delta d\delta \qquad (12)$$

$$\left\langle\left\langle F_D(\mathbf{q},\mathbf{D},\mathbf{R}_D)\right\rangle^2_{D,R_D}\right\rangle_{or} = \int_0^{\pi/2}\left\langle F_{D\parallel}(qR_D\sin\beta(\delta))\right\rangle^2_{R_D}\left\langle F_{D\perp}(qR\cos\beta(\delta))\right\rangle^2_R h(\delta)\sin\delta d\delta \qquad (13)$$

$$\left\langle\left\langle F_1^2(\mathbf{q},\mathbf{D},\mathbf{R}_D)\right\rangle_{D,R_D}\right\rangle_{or} = \int_0^{\pi/2}\left\langle F^2_{D\parallel}(qR_D\sin\beta(\delta))\right\rangle_{R_D}\left\langle F^2_{D\perp}(qR\cos\beta(\delta))\right\rangle_R h(\delta)\sin\delta d\delta \qquad (14)$$

Details of this calculation are outlined in ref.[16] of the main publication.

For the calculations we need to specify the orientational distribution of the cylinders and disks, $h(\delta)$, which is defined by the angle δ between a director given by the unit vector $\mathbf{n}$ and the direction $\mathbf{l}_\parallel$. For the distribution $h(\delta)$ simple approximations can be made which involve Gaussian, Onsager, Boltzmann, or Maier-Saupe distribution functions. These functions are given by

$$h(\delta) = \begin{cases} \exp[-\sin\delta/\overline{\delta}] & , \quad \text{Onsager} \\ \exp[-\delta/\overline{\delta}] & , \quad \text{Boltzmann} \\ \exp[(\cos\delta/\overline{\delta})^2]-1 & , \quad \text{Maier}-\text{Saupe} \\ \exp[-(\delta/\overline{\delta})^2] & , \quad \text{Gaussian} \end{cases} \qquad (15)$$

with $0 \leq \bar{\delta} < \infty$. A value of 0 corresponds to a uniform orientation of all cylinders in the direction of the director **n**, whereas a value of $\bar{\delta} \to \infty$ corresponds to an isotropic distribution. If the distribution function is known, the orientational order parameter *S* defined as

$$S = \left\langle \frac{3\cos^2 \delta - 1}{2} \right\rangle \tag{16}$$

For all scattering patterns a Gaussian-type orientation distribution (Figure S7) gave the best agreement between experiment and simulation. The structural parameters used for the simulations are summarized in Table S1-3.

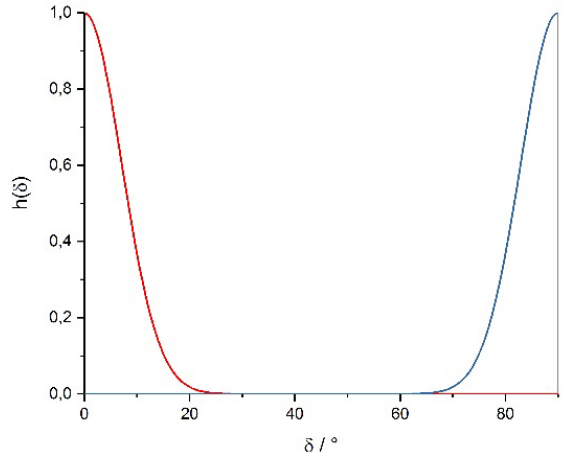

Fig. S7 Gaussian orientational distribution functions. Used for the wormlike micelles and the gold nanorods (red) and the nanoplatelets (blue).

Additionally, 2D-scattering patterns of a pure water microjet with the same diameter and flow rate are shown for the solvent background measurements in Figure S8 to approve that there were no artefacts in the 2D-scattering patterns of the anisotropic particle jets before.

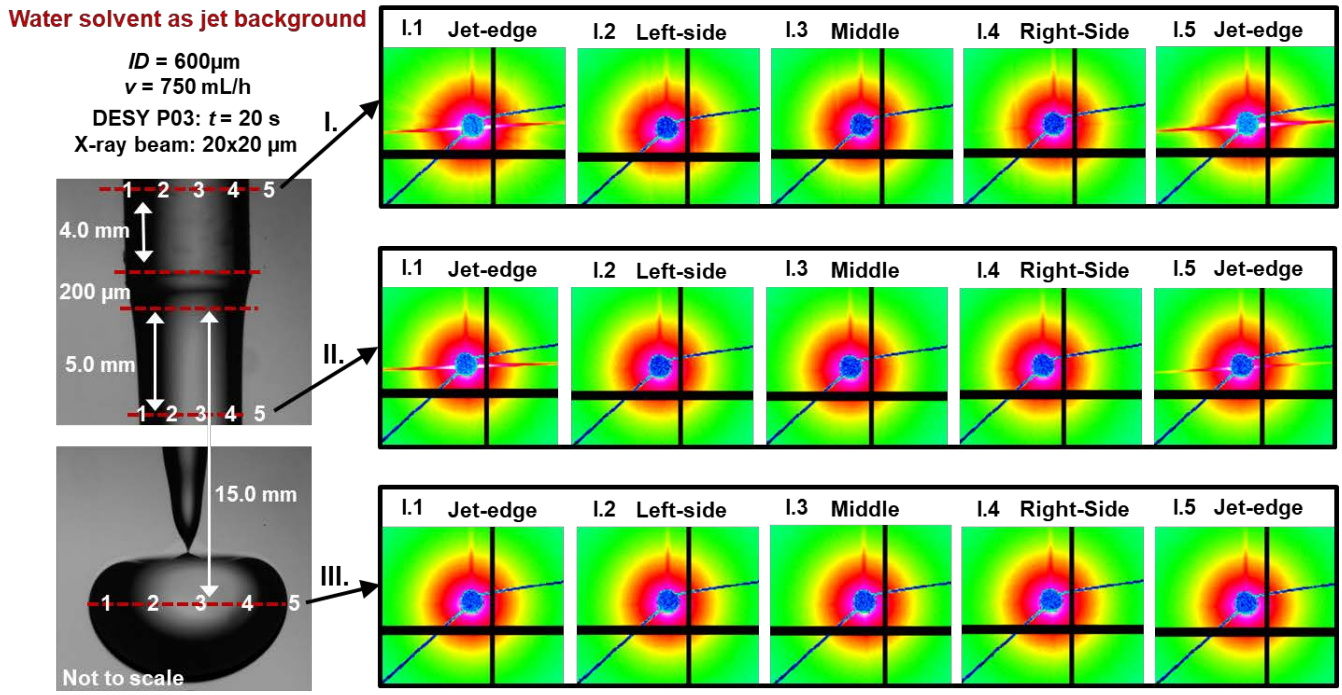

Fig. S8 2D-scattering patterns of a pure water microjet. (I) On the glass capillary 4 mm before outlet, (IV) freejet 5 mm after outlet and (V) droplet region 15 mm after outlet.

Table S1 Parameters for quantitative calculations in Figure 1c and Figure S9b.

3% w/w Hectorite nanoplatelets	**I.1**	**I.4**	**IV.4**	**V.4**
Disk radius, *R*; nm	300	285	160	260
Relative std. deviation, σ_R	0.1	0.1	0.1	0.1
Layer thickness, *d*; nm	1.0	1.0	1.0	1.0
Relative std. deviation, σ_d	0.07	0.07	0.07	0.07
Mean deviation, *dbeta*	10	14	65	10
Orientational parameter, *f*	-0.48	-0.46	-0.14	-0.48
Orientation parameter, *S*	0.92	0.89	0.20	0.92

Table S2 Parameters for quantitative calculations in Figure S10b.

10% w/w Wormlike micelles	**I.1**	**I.4**	**IV.4**	**V.4**
Cylinder length, *L*; nm	30	20	20	15
Relative std. deviation, σ_L	0.1	0.1	0.1	0.1
Cylinder radius, *R*; nm	9	11.5	11.5	12
Relative std. deviation, σ_R	0.07	0.07	0.07	0.07
Unit cell dimension, *a*; nm	42	42	42	42
Radial domain size, D_a; nm	120	55	55	55
Azimuthal coherence length, Dψ; nm	5	48	45	48
Displacement, *σa, nm*	10	6	8	6
Mean deviation, *dbeta*	2	11	55	12
Orienation parameter, *S*	0.98	0.94	0.31	0.93

Table S3 Parameters for quantitative calculations in Figure S11b.

Gold nanorods	**I.1**	**I.4**	**IV.4**	**V.4**
Cylinder length, *L*; nm	71.4	71.4	71.4	71.4
Relative SD, *σL*	0.1	0.1	0.1	0.1
Cylinder radius, *R*; nm	13	13	13	13
Relative SD, *σR*	0.07	0.07	0.07	0.07
Mean deviation, *dbeta*	65	95	99	35
Orienation parameter, *S*	0.23	0.11	0	0.58

Sets of scattering patterns

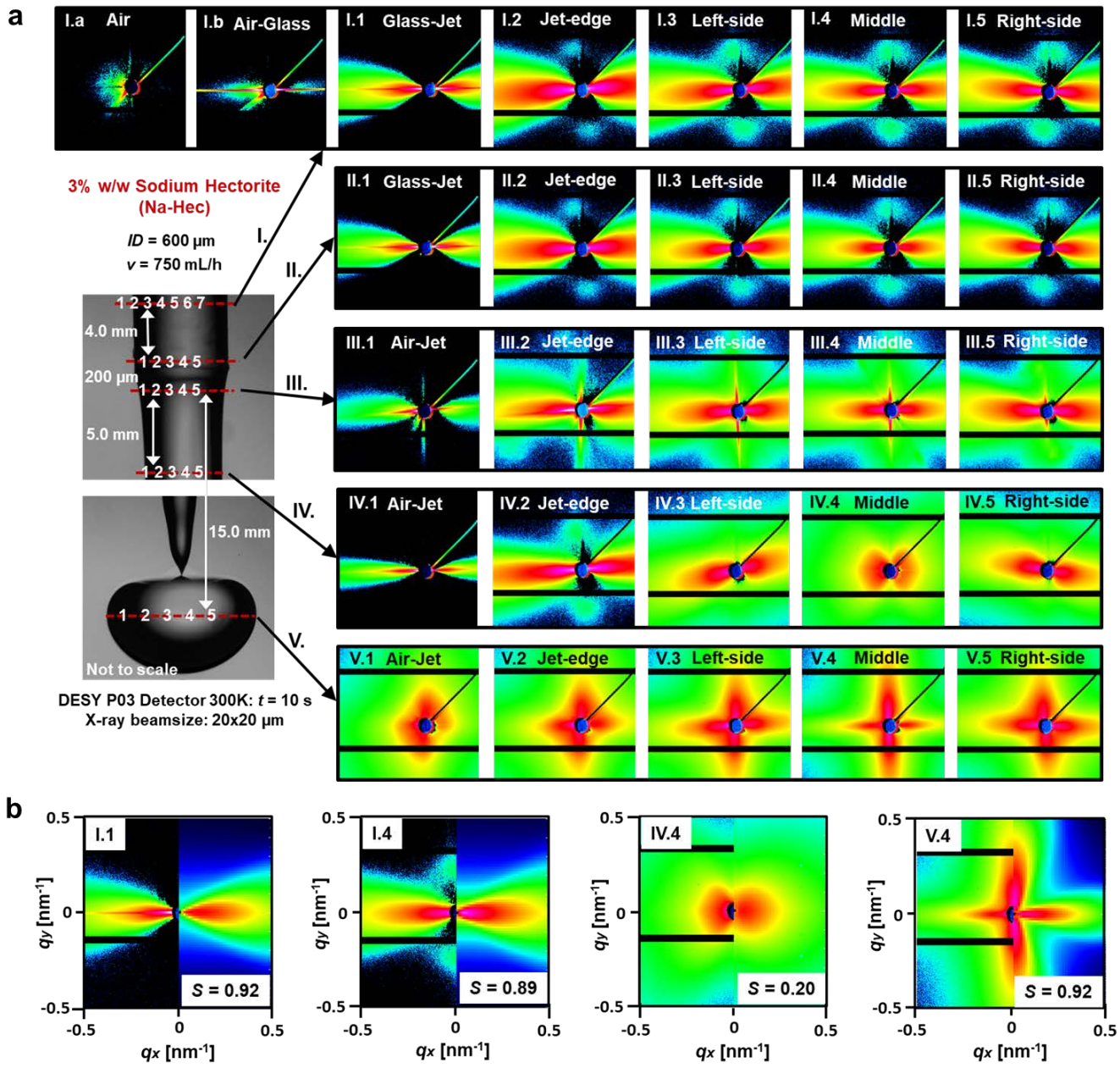

Fig. S9 Sets of measured scattering patterns of the hectorite nanoplatelets. a) At specified scan positions and (b) calculations of scattering patterns as well as their orientation parameter *S* at four characteristic microjet positions.

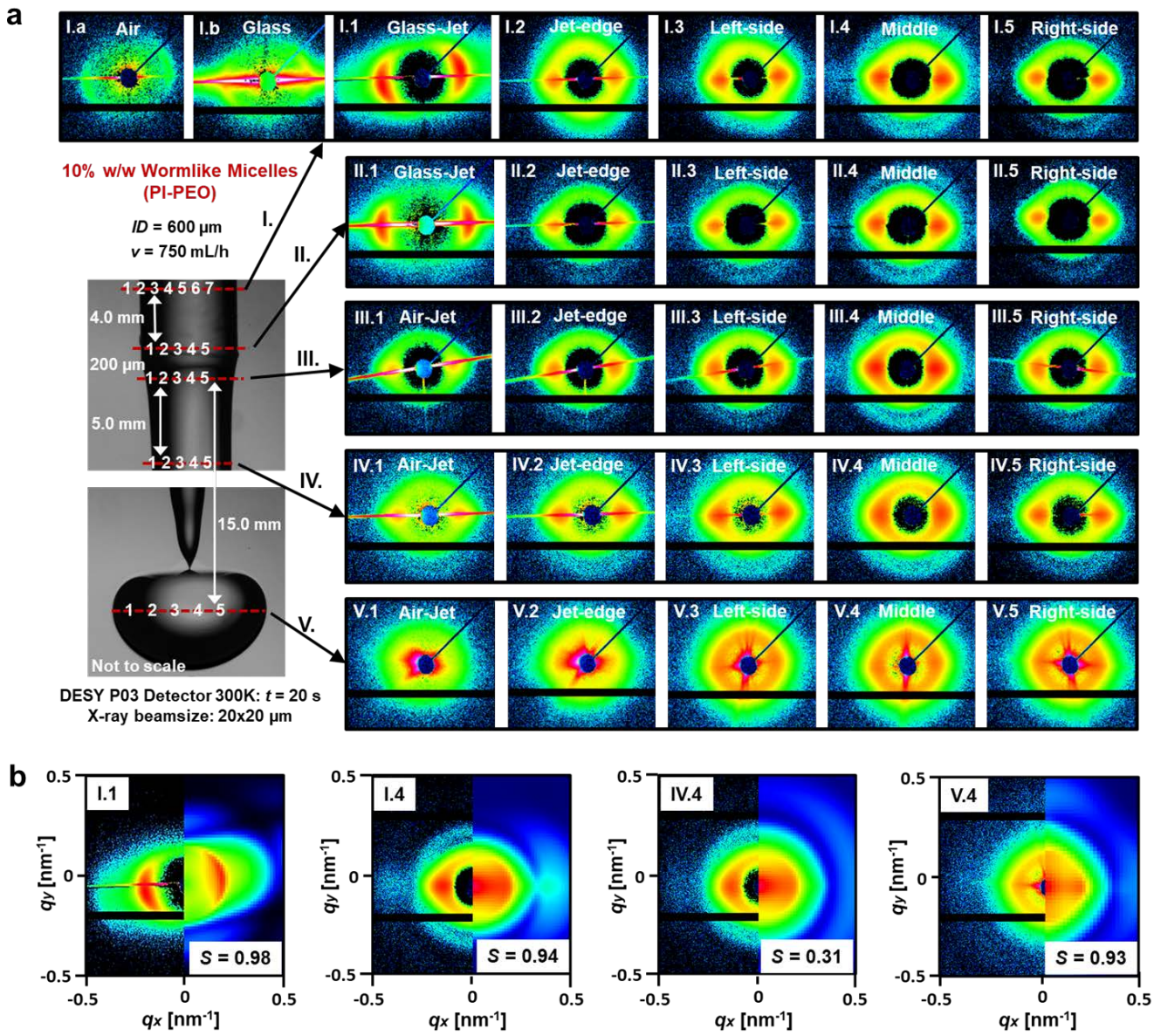

Fig. S10 Sets of measured scattering patterns of the wormlike micelles. a) At specified scan positions and (b) calculations of scattering patterns as well as their orientation parameter *S* at four characteristic microjet positions.

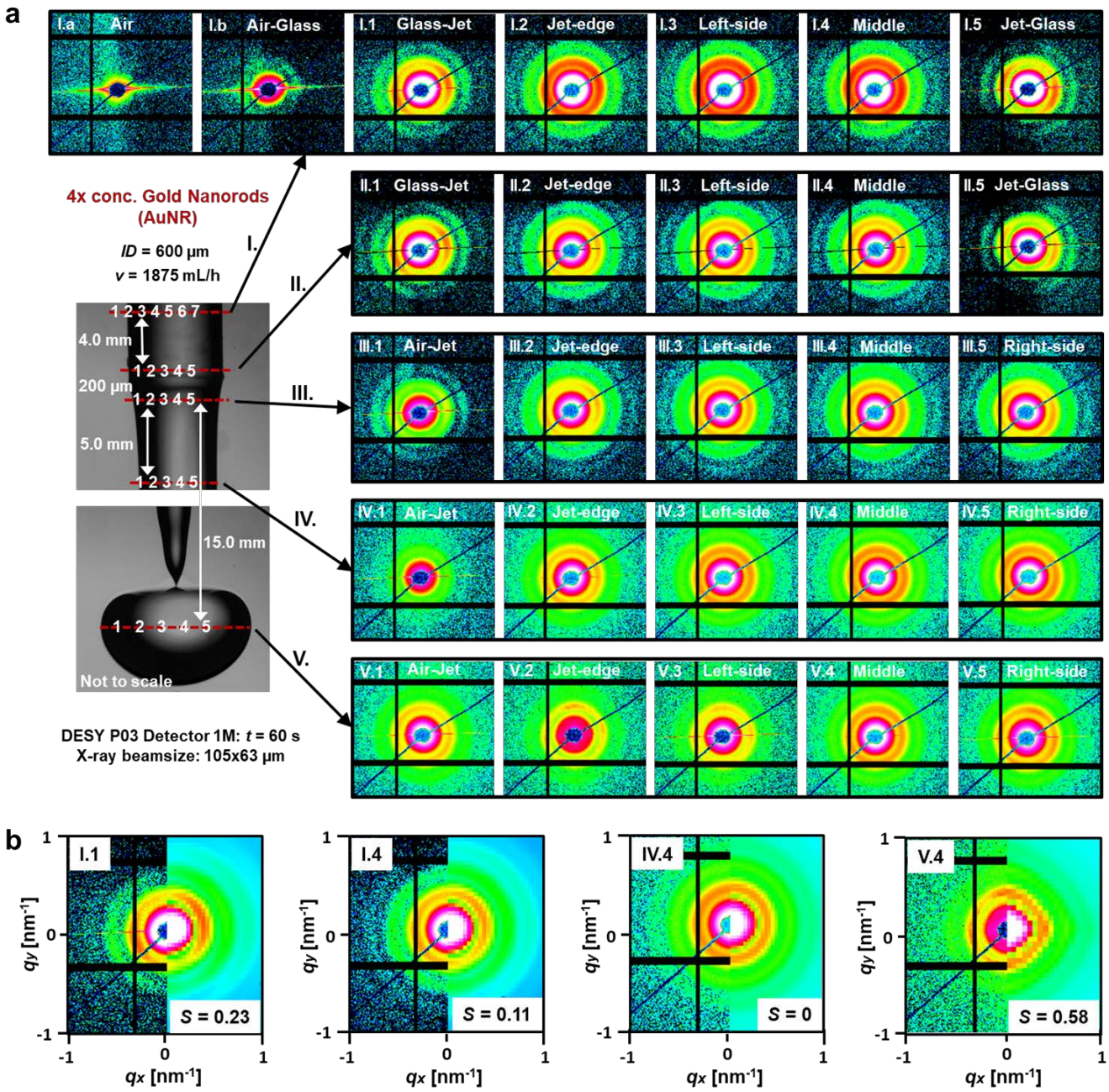

Fig. S11 Sets of measured scattering patterns of the nanorods. a) At specified scan positions and (b) calculations of scattering patterns as well as their orientation parameter *S* at four characteristic microjet positions.